

Enhanced Thermoelectric Properties in a New Silicon Crystal Si₂₄ with Intrinsic Nanoscale Porous Structure

Kisung Chae,^{†,‡} Seoung-Hun Kang,^{†,‡} Seon-Myeong Choi,^{†,||} Duck Young Kim,^{*,‡,§} and Young-Woo Son^{*,†}

HPSTAR
559-2018

[†]Korea Institute for Advanced Study, Seoul 02455, South Korea

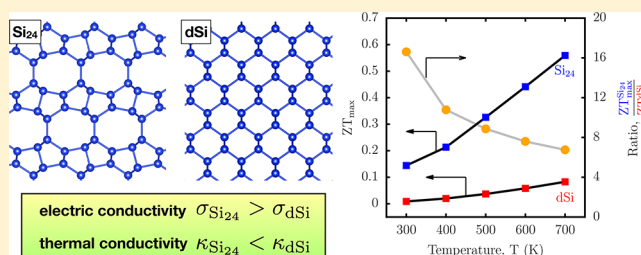
[‡]Center for High Pressure Science & Technology Advanced Research, Shanghai 201203, People's Republic of China

[§]Division of Advanced Nuclear Engineering, POSTECH, Pohang 37673, South Korea

S Supporting Information

ABSTRACT: Thermoelectric device is a promising next-generation energy solution owing to its capability to transform waste heat into useful electric energy, which can be realized in materials with high electric conductivities and low thermal conductivities. A recently synthesized silicon allotrope of Si₂₄ features highly anisotropic crystal structure with nanometer-sized regular pores. Here, based on first-principles study without any empirical parameter we show that the slightly doped Si₂₄ can provide an order-of-magnitude enhanced thermoelectric figure of merit at room temperature, compared with the cubic diamond phase of silicon. We ascribe the enhancement to the intrinsic nanostructure formed by the nanopore array, which effectively hinders heat conduction while electric conductivity is maintained. This can be a viable option to enhance the thermoelectric figure of merit without further forming an extrinsic nanostructure. In addition, we propose a practical strategy to further diminish the thermal conductivity without affecting electric conductivity by confining rattling guest atoms in the pores.

KEYWORDS: First-principles calculations, thermoelectric figure of merit, electron–phonon coupling, intrinsic nanostructure



Thermoelectricity is one of the renewable energy solutions that converts waste heat into viable electric energy without generating greenhouse gases. It creates electric current by thermal motion of charge carriers due to a temperature gradient. Performance of thermoelectric materials can be evaluated through dimensionless figure of merit (ZT)

$$ZT = \frac{\sigma S^2}{\kappa_l + \kappa_e} T \quad (1)$$

which is determined by Seebeck coefficient (*S*), electric conductivity (σ), and thermal conductivities (κ) at a given temperature (*T*). For κ , subscripts *l* and *e* refer to lattice and electronic contributions to heat conduction, respectively. To increase the ZT value, a material needs to be a good electrical conductor as well as a good heat insulator as seen in eq 1. Such a conflicting condition has recently been realized in a layered crystalline material^{1,2} with strong bond anharmonicity, which can be measured by Grüneisen parameter and be a fingerprint for potential thermoelectric materials.

However, it is still challenging to achieve a high ZT in three-dimensional (3D) crystals because the materials properties listed above are coupled to each other. For instance, increasing a charge carrier in 3D semiconductor by doping would increase both σ and κ_e simultaneously. Also, lifetimes of both charge carriers and phonons in a heavily doped material will be

significantly lowered due to increased scattering. In order to overcome this complication, various efforts have been made to reduce the κ_l by postprocessings such as alloying,^{3,4} nanostructuring,^{5–13} and confining rattling guest atoms in cages of skutterudites and clathrates.¹⁴ The alloy and nanostructure, however, might lower the mobility of charge carriers by enhancing impurity/boundary scattering, and the confinement is only valid for porous materials which can host guest atoms.

Aforementioned favorable conditions for a higher ZT can be found in a new silicon allotrope, Si₂₄, with intriguing electronic properties such as quasi-direct bandgap.¹⁵ Specifically, Si₂₄ shows the intrinsic nanostructure as in the case of a good thermoelectric material, SnSe^{1,2} [see Figure 1a,b]. This is in contrast to the previous studies for Si with postprocessings of extrinsic nanoscale structures.^{5–13} Moreover, the Si₂₄ features regular array of nanosized pores as in skutterudites and clathrates, which makes it even more promising as a thermoelectric material. This indicates that an enhanced thermoelectric property can be achieved in a bulk Si material without postprocessings, rendering thermal stability in operating conditions. We note here that Si₂₄ is shown to be

Received: March 23, 2018

Revised: July 3, 2018

Published: July 6, 2018

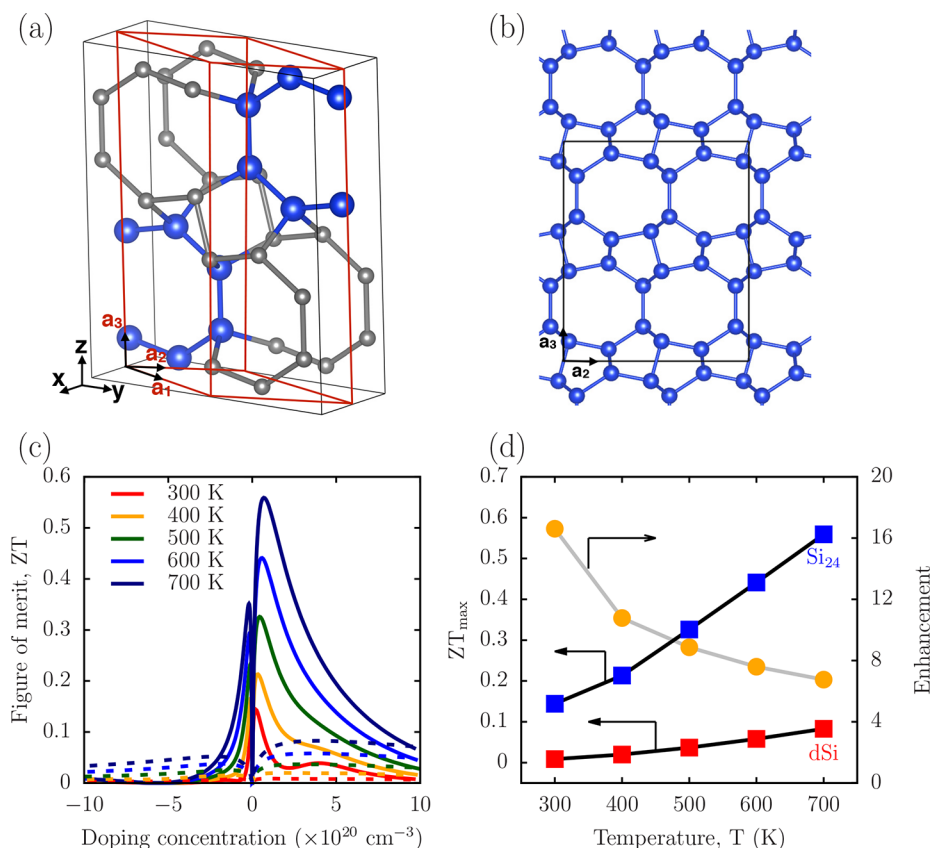


Figure 1. Ball-and-stick models of the Si_{24} crystal with (a) a perspective view and (b) orthogonal projection along the x -axis. (a) The primitive cell and the orthorhombic Bravais unitcell are shown as the red and black parallelepipeds, respectively. Twelve atoms in the primitive cell are shown in large blue balls, while the rest of the atoms are shown as small gray balls. (b) Continuous nanopores are shown where a one-dimensional array of Na ions (not shown) were confined for synthesis. (c) Thermoelectric figure of merit (ZT) of Si_{24} along x -axis are shown in continuous lines as a function of temperature, and the ZT values for dSi are also shown as dashed lines for comparison. Positive and negative doping concentrations (n) refer to that of excess electron and hole, respectively. (d) The maximum values of ZT (ZT_{max}) for a varying temperature are shown as squares, of which the optimum doping concentrations (in 10^{20} cm^{-3}) for Si_{24} are 0.21, 0.35, 0.44, 0.59, and 0.69 for increasing temperature; the values are 0.97, 1.81, 3.12, 3.43, and 4.03 for dSi. The enhancement (ratio of the ZT_{max} for Si_{24} to dSi) is also plotted as orange circles.

stable in a wide range of temperature¹⁵ (~ 750 K) and pressure¹⁶ (~ 8 GPa). We also point out some of the advantages of employing a Si material over other materials containing heavy metal elements (e.g., PbTe) in that Si is cheap, nontoxic, Earth-abundant, and free of phase separation.

Besides, due to the complex interactions involved in the transport phenomena as mentioned above describing transport properties to a reasonable degree remains challenging. Some of the previous studies^{17,18} used too simplified approximations to the electronic relaxation times. For instance, overestimated values of ZT were reported for black phosphorus obtained with a single-valued relaxation time, adapted from the experiment,¹⁷ from a deformation potential theory¹⁹ or from a constant relaxation time approximation.²⁰ When the effects of electron–phonon interactions were explicitly taken into account, the ZT values decreased by orders of magnitude.²¹

In this Letter, we report the enhanced thermoelectric properties of the Si_{24} over the cubic diamond phase counterpart (dSi) by performing various first-principles calculations without using empirical relaxation times of electron and phonon in Si_{24} . Specifically, all of the elastic scattering events between electron and phonon with varying energies and momenta were explicitly enumerated for electric conductivity, σ . Similarly, the anharmonic effects of heat transport due to the three-phonon scattering were explicitly

considered for the lattice thermal conductivity, κ_l . We ascribe the order-of-magnitude enhancement in the ZT to a significant anharmonicity in Si_{24} , which is also confirmed by computing anomalously high Grüneisen parameters. The enhanced ZT of intrinsic Si_{24} is shown to range from 0.14 to 0.6 at 300 to 700 K. This is still smaller than the best record of SnSe at high temperature (from 0.12 to 2.6 at 300 to 923 K)¹ but is comparable to those of postprocessed dSi nanostructure.^{5–13} From these, we expect that gentle manipulations of intrinsic atomic structures of Si_{24} such as rattling effects of guest atoms in the nanopores could enhance the thermoelectric performance further by reducing the lattice thermal conductivities, thus enabling the new silicon crystal be a fruitful playground to engineer thermoelectric properties.

To describe the reliable thermoelectric properties for Si_{24} using first-principles calculations, we performed density functional theory calculations as implemented in Quantum Espresso package.²² We used norm-conserving pseudopotentials²³ with the plane wave kinetic energy cutoff of 60 Ry (816.34 eV) and exchange–correlation functional of Perdew–Burke–Ernzerhof²⁴ (PBE) within generalized gradient approximation was used. In order to evaluate the σ explicitly from first-principles calculations, the phonon-mediated σ was evaluated by using the transport Eliashberg spectral function^{25,26} as implemented in EPW package.²⁷ The Bloch wave

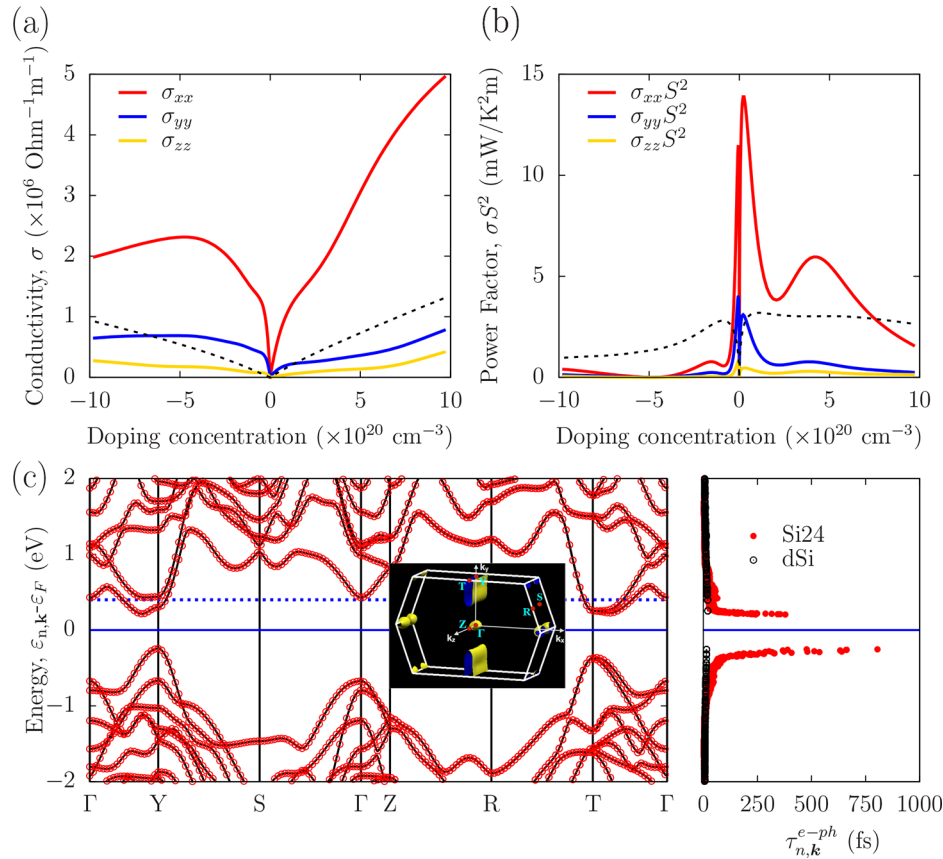


Figure 2. (a) Electrical conductivity tensor components and (b) power factor at 300 K with a varying doping concentration. The continuous and dashed lines are for Si₂₄ and dSi, respectively. (c) Electronic band dispersion of Si₂₄ from first-principles calculations (black lines) and maximally localized Wannier functions (MLWFs) (red circles). Relaxation times ($\tau_{n,k}^{e-ph}$) as in eq 2 of electrons at 300 K for both Si₂₄ and dSi are also provided aside. In the inset, the Fermi surface in the Brillouin zone of Si₂₄ at a doping concentration of $2.5 \times 10^{20} \text{ cm}^{-3}$, which is marked as blue dotted line in (c). In (c), the zero energy denoted by a solid horizontal line was set to be middle between conduction and valence band edges.

function calculated on a Γ -centered k/q -point mesh of $10 \times 10 \times 6$ was interpolated to a much denser grid of $40 \times 40 \times 9$ by using the maximally localized Wannier functions (MLWFs).^{28–30} Using the MLWFs, the relaxation time ($\tau_{n,k}^{e-ph}$) by electron–phonon coupling were computed on the denser k/q grids as

$$\frac{1}{\tau_{n,k}^{e-ph}} = \frac{2\pi}{N} \sum_{m,\lambda,q} \left| g_{m,n}^{k,\lambda} \right|^2 [\delta(\varepsilon_{m,k} - \varepsilon_{n,k} + \omega_{\lambda,q})(n_{\lambda,q} + f_{m,k}) + \delta(\varepsilon_{m,k} - \varepsilon_{n,k} - \omega_{\lambda,q})(n_{\lambda,q} - f_{m,k} + 1)] \quad (2)$$

where $\omega_{\lambda,q}$ is the energy of a phonon with polarization λ and wave vector q in the Brillouin zone (BZ), and $n_{\lambda,q}$ and $f_{m,k}$ are Bose–Einstein and Fermi–Dirac distribution functions, respectively. N is the total number of k/q grid points in the BZ. The $\varepsilon_{n,k}$ is energy of a Bloch state at n th band at k point in the BZ.³¹ The $g_{m,n}^{k,\lambda}$ is an electron–phonon coupling matrix element, which is computed as $\langle \Psi_{m,k+q} | \partial_{\lambda,q} V | \Psi_{n,k} \rangle$. $\Psi_{n,k}$ is a Kohn–Sham wave function, and $\partial_{\lambda,q} V$ is the variation of the Kohn–Sham potential for a unit displacement of the nuclei along the phonon mode of polarization λ and wave vector q . Using the $\tau_{n,k}^e \approx \tau_{n,k}^{e-ph}$ as in eq 2, electron transport coefficients were calculated by using bolztrap code³² within semiclassical Boltzmann transport equation: i.e., $\sigma_{\alpha\beta}(\varepsilon) = \frac{e^2}{N} \sum_{n,k} \tau_{n,k}^{e-ph} v_{\alpha,n,k} v_{\beta,n,k} \left(-\frac{\partial f_{n,k}}{\partial \varepsilon} \right)$, where $\alpha, \beta = x, y,$

or z and N is the number of k -points in the BZ. The $v_{\alpha,n,k}$ is a group velocity of electrons at $\varepsilon_{n,k}$ along α . Note that other contributions for σ such as electron–electron and impurity scattering are assumed to be negligible (see SI S1). The Seebeck coefficient, S , shown in eq 1 was calculated from the Mott formula at the Fermi level as

$$S = \frac{\pi^2 k_B^2 T}{3e} \frac{d(\log(\sigma))}{d\varepsilon} \Big|_{\varepsilon=\varepsilon_F}$$

where e and k_B are the charge of an electron and Boltzmann’s constant, respectively. The electronic contribution to the thermal conductivity (κ_e) was evaluated via Wiedemann–Franz law:³³ $\kappa_e = L_0 \sigma T$ with $L_0 = 2.44 \times 10^{-8} \text{ W}\cdot\text{ohm}/\text{K}^2$. The κ_e computed with Wiedemann–Franz law is exact under the assumptions we used above (i.e., $\tau_{n,k}^e \approx \tau_{n,k}^{e-ph}$) because diffusive motion of electron gas is described by Boltzmann transport equation with relaxation time approximation.

Similarly, the lattice thermal conductivity (κ_l) with anharmonic effects between three phonons was computed by solving Boltzmann transport equation as implemented in phono3py code.³⁴ The third-order interatomic force constants were evaluated for dynamical matrix by a finite displacement method with a displacement and distance cutoff of 0.03 and 15 Å, respectively. In a $(3 \times 3 \times 2)$ supercell with 216 Si atoms, a total of 12,108 displaced configurations were generated. Hellmann–Feynman forces in each configuration was computed by first-principles calculations by using Vienna ab

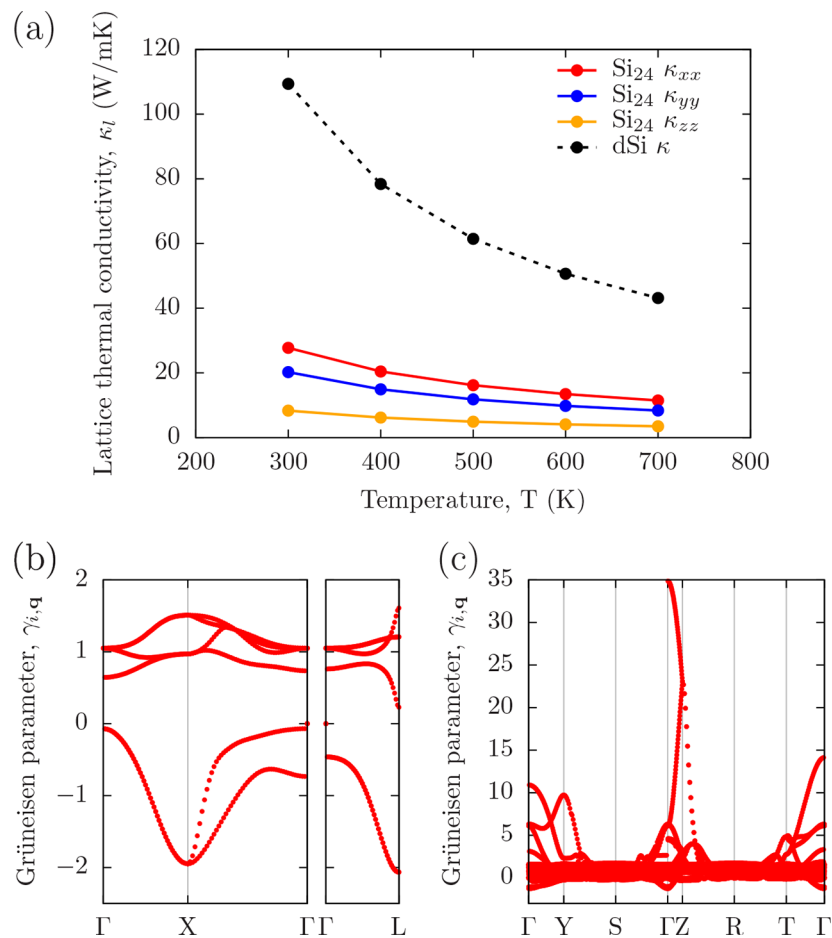


Figure 3. (a) Lattice thermal conductivity (κ_l) due to anharmonic phonons. Grüneisen parameters for (b) dSi and (c) Si_{24} are shown.

initio software package^{35–38} with projector augmented wave method³⁹ and PBE exchange-correlation functional.²⁴ Plane wave was expanded with the kinetic cutoff energy of 400 eV, and Γ -centered $9 \times 9 \times 3$ grid points in the BZ were used for the primitive cell of Si_{24} . After all the force evaluation, the κ_l was evaluated by integrating over q points in the full BZ of $14 \times 14 \times 14$ grid points.

The Si_{24} crystal features an open-channel structure along a crystallographic axis (x) as shown in Figure 1a,b. Each of the channels of which the diameter is approximately 0.54 nm is composed of eight-membered-rings of distorted sp^3 Si bonds. When compared to the dSi having the ideal sp^3 bonding character with the distance of 2.35 Å and with the angle of 109.5° , those in Si_{24} range from 2.33 to 2.41 Å, and from 97.73° to 135.63° , respectively.¹⁵ In particular, the open-channel structure is attributed to its two-step synthesis process such that a high pressure phase of $\text{Na}_4\text{Si}_{24}$ compound is initially synthesized and pressurized at a hydrostatic pressure of 10 GPa and that only loosely captured Na atoms in the cage are selectively removed from the compound at ambient pressure.¹⁵ As a result, the structure with a regular array of one-dimensional nanopores is retained as seen in Figure 1b. Note that the structure is highly anisotropic owing to the open channels. For instance, when comparing densities along different orientations of the crystal Si_{24} shows denser atomic arrangement along the x -axis unlike the others, which significantly differs from isotropic atomic arrangement for dSi.

We investigate thermoelectric properties of Si_{24} for various temperatures up to 700 K since thermal stability of Si_{24} in air was experimentally confirmed up to 750 K.¹⁵ The ZT obtained from our calculations indicates that Si_{24} shows superior thermoelectric properties compared to dSi, especially when lightly doped with electrons as shown in Figure 1c. The overall ZT values are enhanced with an increasing temperature for both Si_{24} and dSi. On the other hand, enhancement factor, defined as a ratio of the maximum ZT (ZT_{max}) between Si_{24} and dSi, decreases as temperature increases, which reaches ~ 17 at 300 K. The optimal doping concentration for the ZT_{max} increases with temperature as in Figure 1c. We note that overall values of the optimal doping concentration are much smaller for Si_{24} than dSi. This is advantageous because impurity scattering becomes significant for heavily doped semiconductors, of which the effects are difficult to be captured directly in the first-principles calculations.

It is worth noting here a constant relaxation time approximation can lead to inaccurate ZT value.¹⁸ As is known for other materials,²¹ elaborated description of electron–phonon coupling tends to correct the overestimated ZT values obtained from simplified calculations. Likewise, the momentum dependence of relaxation time in eq 2 needs to be taken into account in evaluating the electrical conductivity σ to obtain a reliable ZT, specifically for a newly synthesized material. Another point to note is that evaluation of accurate σ values requires remarkably dense k/q grid points, and convergence test should be performed with caution. We

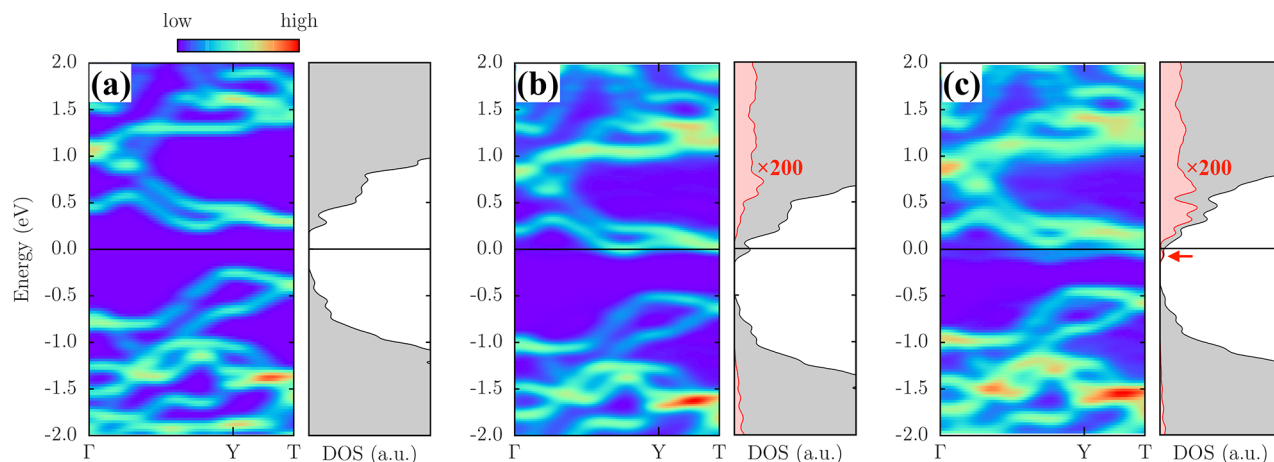


Figure 4. Electronic band dispersions and density of states of Na-doped Si_{24} with (a) 0, (b) 1, and (c) 2 Na ions in a $(3 \times 2 \times 2)$ supercell containing 288 Si atoms. The supercell band structures are unfolded to the irreducible Brillouin zone of the primitive cell of Si_{24} by using BandUP code.^{45,46} Color-coding indicates spectral weight. Total and projected DOS to Na (magnified by a factor of 200) are shown in gray and red shades, respectively. For a single Na ion content, the ionic doping concentration corresponds to $1.58 \times 10^{20} \text{ cm}^{-3}$. In (a), the zero energy of the pristine Si_{24} was set to be the middle between edges of conduction and valence bands and was set to be charge neutral points due to Na atom doping for both (b,c).

confirmed that the data grid used here ($40 \times 40 \times 9 = 14,400$) gives reasonably converged ZT values less than 5% relative error compared to that from the most dense grid mesh we tested ($50 \times 50 \times 9 = 22,500$). The detailed results are provided in SI S2.

To explain the enhanced ZT of Si_{24} , we will discuss the effects of each of the components in ZT hereafter. First, we consider the effects of electronic contributions to the thermoelectric properties. We find that the electrical conductivity (σ) of Si_{24} is highly anisotropic (Figure 2a), which can be deduced from its anisotropic geometry (Figure 1a). Compared with the dSi, it is remarkable that the σ_{xx} for Si_{24} is always higher throughout the doping range considered in this study, whereas σ_{yy} and σ_{zz} are largely suppressed. Note that the nanopores run along the x -axis (Figure 1b) where the atomic arrangement is most densely packed. In contrast, along the orientations perpendicular to the nanopore axis, electrons are more likely to be scattered by electron–phonon coupling due to the anisotropic bonding.

Similarly, power factors (σS^2) also show the high anisotropy as observed in the electric conductivity (Figure 2b). In this case, however, the magnitude of the σS^2 also varies significantly due to carrier type and density. When Si_{24} is lightly doped by electrons, the $\sigma_{xx} S^2$ reaches the maximum, significantly exceeding that of the dSi (Figure 2b). For higher doping concentration, the $\sigma_{xx} S^2$ drops substantially and becomes smaller than that of dSi. For hole doping, the σS^2 in all directions are significantly diminished compared to the electron-doped cases and become much smaller than that of dSi except for the peaks at low concentration. As the power factor is linearly proportional to the ZT, this agrees well with the above observation that ZT reaches the maximum at light electron doping as in Figure 1c.

These improved thermoelectric properties of Si_{24} can be ascribed to its electronic band dispersions (Figure 2c). With small electron doping concentration as marked in Figure 2c, there exist multiple electron pockets (or valleys) in the BZ as can be also seen in the Fermi surface at that doping level; see the inset of Figure 2c. This multiple valley degeneracy is also known to be responsible for the good thermoelectric

performance of $\text{PbTe}_{1-x}\text{Se}_x$.⁴⁰ The highly anisotropic electronic structures are clearly seen in Si_{24} from the Fermi surface, which is consistent with the anisotropic crystal structure. Note that the relaxation times in Si_{24} are much longer than those in dSi, especially for low energies, or low doping levels. This agrees with the fact that high ZT_{max} of Si_{24} occurs at much lower doping concentration than that of dSi as shown in Figure 1c.

Furthermore, Si_{24} provides low lattice thermal conductivity (κ_l) as seen in Figure 3a, which renders even better thermoelectric performance compared to dSi. The calculated κ_l for Si_{24} is approximately 4 times lower than that of dSi along x -axis throughout the temperature range in this study. The difference becomes even greater to be ~ 13 times for the κ_l along z -axis. If we consider electronic contribution to the thermal conductivity via Wiedemann–Franz law, the anisotropy in heat conduction becomes even greater due to higher electrical conductivity along the x -axis compared to the z -axis.

We show the Grüneisen parameter for both crystals in Figure 3b,c, which is a measure of anharmonicity of the bonds. The resistivity of the heat conduction through the lattice vibrations due to the Umklapp process increases with the magnitudes of Grüneisen parameters. The highest Grüneisen parameters shown along the Γ -Z path indicate that the anharmonic scattering of phonons occurs mostly along the z -direction, and agrees with the lowest κ_l along z -direction (Figure 3a).

For practical aspects of its thermoelectric application, we discuss the effects of conventional defects on transport properties of Si_{24} . First of all, recent experiment¹⁶ and theoretical calculations¹⁵ of Raman spectra agree well with each other in a wide range of temperature and pressure. From these, we could infer that the local atomic structures of synthesized Si_{24} samples are quite close to the ideal ones. Moreover, a recent theoretical work on various defects in Si_{24} ⁴¹ revealed that population of substitutional dopants are dominant over intrinsic point defects such as vacancy and interstitial thanks to their relatively lower formation energies ($< 0.7 \text{ eV}$) compared with the intrinsic ones (2.3–3.7 eV). It is noteworthy that the typical n-type dopant states with very low

ionization energy hybridize with conduction bands,⁴¹ realizing good electric conductivity of the doped Si₂₄.

We further discuss the effects of remaining guest atoms in the cages of Si₂₄. As we mentioned above, the Si₂₄ crystal is synthesized by removing Na atoms confined in the cages of Na₄Si₂₄, which takes ~8 days at 400 K.¹⁵ This indicates that on one hand the Na atoms are loosely bound to the host Si atoms similar to clathrates, so that the trapped guest atoms can escape from the crystal. On the other hand, the relatively slow degassing process even at an elevated temperature is attributed to the high kinetic energy barrier for migration of Na atoms in the channel from one cage to the adjacent one. On the basis of our nudged elastic band calculations, the barrier is estimated to be ~1 eV, which is in a good agreement to the literature.⁴² In addition, when comparing the size of the channel windows and Na atom, the transport behavior of the guest atoms is dominated by a single-file diffusion of which the degassing rate is limited by diffusive motion of the atoms at the ends of the line. Thus, complete removal of the Na atoms might be difficult and residual Na atoms might be remaining in the cages.

We expect that those residual guest atoms would have the rattling effects as observed in skutterudites and clathrates,¹⁴ enhancing the thermoelectric properties of the crystal. With the guest atoms, their thermal vibrations can interact with the acoustic phonons of the host atoms, which suppresses the lattice thermal conductivity further. Similarly, thermal conductivities of carbon nanotubes (CNTs) filled with water was suppressed by 20–35% compared to that of empty CNT.⁴³ Our equilibrium molecular dynamics simulations clearly indicate that the lattice thermal conductivity is reduced by at least ~50% due to Na ions in the pores for Na_{0.37}Si₂₄ as shown in SI S3.

In addition, the residual Na atoms in the channel would donate electrons to the host Si₂₄ crystal without affecting the electronic structures. For instance, band structures in Figure 4 are nearly unchanged for a single Na atom out of 288 Si atoms (~0.35 atom %), and donor level begins to appear when two Na atoms are doped (~0.7 atom %) as indicated by the arrow. This spontaneous electron doping is advantageous for the Si₂₄ to be used as a TE material as discussed above (see Figure 1c,d). Moreover, this spontaneous doping effect would significantly lower the chances of electrons being scattered by impurities (i.e., dopant atoms), which becomes dominant at heavy doping. It is worth to note that large number of guest atoms would donate many electrons to the cage structure and eventually turn the host materials into a metal.⁴⁴ In this case, thermal transport is dominated by electrons, i.e., $\kappa \approx \kappa_e$.

In conclusion, we demonstrate thermoelectric properties of a new silicon allotrope, Si₂₄ by using various ab initio computational methods without empirical parameters: phonon-mediated electrical conductivity and lattice thermal conductivity with anharmonic phonon effects. The highly anisotropic structure of the Si₂₄ results in anisotropic electronic and thermal transport properties as well. The electron-doped Si₂₄ displays superior thermoelectric behavior to the Si in a cubic diamond phase, which is ascribed to the enhanced power factor and reduced lattice thermal conductivity. We also pointed out that the thermoelectric performance can be further enhanced by guest atoms in the cage due to their role as electron donor and rattler.

■ ASSOCIATED CONTENT

Supporting Information

The Supporting Information is available free of charge on the ACS Publications website at DOI: 10.1021/acs.nanolett.8b01176.

Discussion on electric conductivity; convergence tests for Brillouin zone integration on a discrete grid; rattling effects of Na ions in pores of Si₂₄ (PDF)

■ AUTHOR INFORMATION

Corresponding Authors

*E-mail: duckyoung.kim@hpstar.ac.cn. Phone: +86-21-8017-7094.

*E-mail: hand@kias.re.kr. Phone: +82-2-958-3720. Fax: +82-2-958-3820.

ORCID

Kisung Chae: 0000-0003-1628-408X

Present Address

^{||}(S.-M.C.) Samsung Advanced Institute of Technology, Suwon 13595, South Korea.

Author Contributions

[†]K.C. and S.-H.K. contributed equally to this work.

Notes

The authors declare no competing financial interest.

■ ACKNOWLEDGMENTS

We thank Korea Institute for Advanced Study for providing computing resources (KIAS Center for Advanced Computation Linux Cluster System) for this work. Y.-W.S. was supported by NRF of Korea (Grant 2017R1A5A1014862, SRC program: vdWMRC Center). D.Y.K. acknowledges the support by NSFC of China (Grant 11774015) and NRF (NRF-2017R1D1A1B03031913).

■ REFERENCES

- (1) Zhao, L.-D.; Lo, S.-H.; Zhang, Y.; Sun, H.; Tan, G.; Uher, C.; Wolverton, C.; Dravid, V. P.; Kanatzidis, M. G. Ultralow thermal conductivity and high thermoelectric figure of merit in SnSe crystals. *Nature* **2014**, *508*, 373–377.
- (2) Zhao, L.-D.; Tan, G.; Hao, S.; He, J.; Pei, Y.; Chi, H.; Wang, H.; Gong, S.; Xu, H.; Dravid, V. P.; Uher, C.; Snyder, G. J.; Wolverton, C.; Kanatzidis, M. G. Ultrahigh power factor and thermoelectric performance in hole-doped single-crystal SnSe. *Science* **2016**, *351*, 141–144.
- (3) Dughaish, Z. H. Lead telluride as a thermoelectric material for thermoelectric power generation. *Phys. B* **2002**, *322*, 205–223.
- (4) Yamashita, O.; Tomiyoshi, S.; Makita, K. Bismuth telluride compounds with high thermoelectric figures of merit. *J. Appl. Phys.* **2003**, *93*, 368–374.
- (5) Lee, J.-H.; Galli, G. A.; Grossman, J. C. Nanoporous Si as an Efficient Thermoelectric Material. *Nano Lett.* **2008**, *8*, 3750–3754.
- (6) He, Y.; Donadio, D.; Lee, J.-H.; Grossman, J. C.; Galli, G. Thermal Transport in Nanoporous Silicon: Interplay between Disorder at Mesoscopic and Atomic Scales. *ACS Nano* **2011**, *5*, 1839–1844.
- (7) Boukai, A. I.; Bunimovich, Y.; Tahir-Kheli, J.; Yu, J.-K.; Goddard, W. A., III; Heath, J. R. Silicon nanowires as efficient thermoelectric materials. *Nature* **2008**, *451*, 168–171.
- (8) Hochbaum, A. I.; Chen, R.; Delgado, R. D.; Liang, W.; Garnett, E. C.; Najarian, M.; Majumdar, A.; Yang, P. Enhanced thermoelectric performance of rough silicon nanowires. *Nature* **2008**, *451*, 163–167.
- (9) Lee, H. J.; Anoop, G.; Lee, H. J.; Kim, C.; Park, J.-W.; Choi, J.; Kim, H.; Kim, Y.-J.; Lee, E.; Lee, S.-G.; Kim, Y.-M.; Lee, J.-H.; Jo, J. Y.

Enhanced thermoelectric performance of PEDOT: PSS/PANI-CSA polymer multilayer structures. *Energy Environ. Sci.* **2016**, *9*, 2806–2811.

(10) Joshi, G.; Lee, H.; Lan, Y.; Wang, X.; Zhu, G.; Wang, D.; Gould, R. W.; Cuff, D. C.; Tang, M. Y.; Dresselhaus, M. S.; Chen, G.; Ren, Z. Enhanced Thermoelectric Figure-of-Merit in Nanostructured p-type Silicon Germanium Bulk Alloys. *Nano Lett.* **2008**, *8*, 4670–4674.

(11) Wang, X. W.; Lee, H.; Lan, Y. C.; Zhu, G. H.; Joshi, G.; Wang, D. Z.; Yang, J.; Muto, A. J.; Tang, M. Y.; Klatsky, J.; Song, S.; Dresselhaus, M. S.; Chen, G.; Ren, Z. F. Enhanced thermoelectric figure of merit in nanostructured n-type silicon germanium bulk alloy. *Appl. Phys. Lett.* **2008**, *93*, 193121.

(12) Tang, J.; Wang, H.-T.; Lee, D. H.; Fardy, M.; Huo, Z.; Russell, T. P.; Yang, P. Holey Silicon as an Efficient Thermoelectric Material. *Nano Lett.* **2010**, *10*, 4279–4283.

(13) Nakamura, Y.; Isogawa, M.; Ueda, T.; Yamasaka, S.; Matsui, H.; Kikkawa, J.; Ikeuchi, S.; Oyake, T.; Hori, T.; Shiomu, J.; Sakai, A. Anomalous reduction of thermal conductivity in coherent nanocrystal architecture for silicon thermoelectric material. *Nano Energy* **2015**, *12*, 845–851.

(14) Dolyniuk, J.-A.; Owens-Baird, B.; Wang, J.; Zaikina, J. V.; Kovnir, K. Clathrate thermoelectrics. *Mater. Sci. Eng., R* **2016**, *108*, 1–46.

(15) Kim, D. Y.; Stefanoski, S.; Kurakevych, O. O.; Strobel, T. A. Synthesis of an open-framework allotrope of silicon. *Nat. Mater.* **2015**, *14*, 169–173.

(16) Tong, X.; Xu, X.; Fultz, B.; Zhang, H.; Strobel, T. A.; Kim, D. Y. Phonons in Si₂₄ at simultaneously elevated temperature and pressure. *Phys. Rev. B: Condens. Matter Mater. Phys.* **2017**, *95*, 094306.

(17) Zhang, J.; Liu, H. J.; Cheng, L.; Wei, J.; Liang, J. H.; Fan, D. D.; Jiang, P. H.; Sun, L.; Shi, J. High thermoelectric performance can be achieved in black phosphorus. *J. Mater. Chem. C* **2016**, *4*, 991–998.

(18) Ouyang, T.; Zhang, P.; Xiao, H.; Tang, C.; Li, J.; He, C.; Zhong, J. Potential thermoelectric material open framework Si₂₄ from a first-principles study. *J. Phys. D: Appl. Phys.* **2017**, *50*, 425501.

(19) Qin, G.; Yan, Q.-B.; Qin, Z.; Yue, S.-Y.; Cui, H.-J.; Zheng, Q.-R.; Su, G. Hinge-like structure induced unusual properties of black phosphorus and new strategies to improve the thermoelectric performance. *Sci. Rep.* **2015**, *4*, 6922.

(20) Zhang, J.; Liu, H. J.; Cheng, L.; Wei, J.; Liang, J. H.; Fan, D. D.; Shi, J.; Tang, X. F.; Zhang, Q. J. Phosphorene nanoribbon as a promising candidate for thermoelectric applications. *Sci. Rep.* **2015**, *4*, 4033.

(21) Liao, B.; Zhou, J.; Qiu, B.; Dresselhaus, M. S.; Chen, G. *Ab initio* study of electron-phonon interaction in phosphorene. *Phys. Rev. B: Condens. Matter Mater. Phys.* **2015**, *91*, 235419.

(22) Giannozzi, P.; Baroni, S.; Bonini, N.; Calandra, M.; Car, R.; Cavazzoni, C.; Ceresoli, D.; Chiarotti, G. L.; Cococcioni, M.; Dabo, I.; Corso, A. D.; de Gironcoli, S.; Fabris, S.; Fratesi, G.; Gebauer, R.; Gerstmann, U.; Gougoussis, C.; Kokalj, A.; Lazzeri, M.; Martin-Samos, L.; Marzari, N.; Mauri, F.; Mazzarello, R.; Paolini, S.; Pasquarello, A.; Paulatto, L.; Sbraccia, C.; Scandolo, S.; Sclauzero, G.; Seitsonen, A. P.; Smogunov, A.; Umari, P.; Wentzcovitch, R. M. QUANTUM ESPRESSO: a modular and open-source software project for quantum simulations of materials. *J. Phys.: Condens. Matter* **2009**, *21*, 395502.

(23) Troullier, N.; Martins, J. L. Efficient pseudopotentials for plane-wave calculations. *Phys. Rev. B: Condens. Matter Mater. Phys.* **1991**, *43*, 1993–2006.

(24) Perdew, J. P.; Burke, K.; Ernzerhof, M. Generalized Gradient Approximation Made Simple. *Phys. Rev. Lett.* **1996**, *77*, 3865–3868.

(25) Allen, P. B. New method for solving Boltzmann's equation for electrons in metals. *Phys. Rev. B: Condens. Matter Mater. Phys.* **1978**, *17*, 3725–3734.

(26) Park, C.-H.; Bonini, N.; Sohler, T.; Samsonidze, G.; Kozinsky, B.; Calandra, M.; Mauri, F.; Marzari, N. Electron-Phonon Interactions and the Intrinsic Electrical Resistivity of Graphene. *Nano Lett.* **2014**, *14*, 1113–1119.

(27) Noffsinger, J.; Giustino, F.; Malone, B. D.; Park, C.-H.; Louie, S. G.; Cohen, M. L. EPW: A program for calculating the electron-phonon coupling using maximally localized Wannier functions. *Comput. Phys. Commun.* **2010**, *181*, 2140–2148.

(28) Marzari, N.; Mostofi, A. A.; Yates, J. R.; Souza, I.; Vanderbilt, D. Maximally localized Wannier functions: Theory and applications. *Rev. Mod. Phys.* **2012**, *84*, 1419–1475.

(29) Souza, I.; Marzari, N.; Vanderbilt, D. Maximally localized Wannier functions for entangled energy bands. *Phys. Rev. B: Condens. Matter Mater. Phys.* **2001**, *65*, 035109.

(30) Marzari, N.; Vanderbilt, D. Maximally localized generalized Wannier functions for composite energy bands. *Phys. Rev. B: Condens. Matter Mater. Phys.* **1997**, *56*, 12847–12865.

(31) Giustino, F.; Cohen, M. L.; Louie, S. G. Electron-phonon interaction using Wannier functions. *Phys. Rev. B: Condens. Matter Mater. Phys.* **2007**, *76*, 165108.

(32) Madsen, G. K. H.; Singh, D. J. BoltzTraP. A code for calculating band-structure dependent quantities. *Comput. Phys. Commun.* **2006**, *175*, 67–71.

(33) Ziman, J. M. *Electrons and Phonons; The Theory of Transport Phenomena in Solids*; Oxford University Press, 1962.

(34) Togo, A.; Chaput, L.; Tanaka, I. Distributions of phonon lifetimes in Brillouin zones. *Phys. Rev. B: Condens. Matter Mater. Phys.* **2015**, *91*, 094306.

(35) Kresse, G.; Hafner, J. *Ab initio* molecular dynamics for liquid metals. *Phys. Rev. B: Condens. Matter Mater. Phys.* **1993**, *47*, 558–561.

(36) Kresse, G.; Hafner, J. *Ab initio* molecular-dynamics simulation of the liquid-metal-amorphous-semiconductor transition in germanium. *Phys. Rev. B: Condens. Matter Mater. Phys.* **1994**, *49*, 14251–14269.

(37) Kresse, G.; Furthmüller, J. Efficiency of *ab-initio* total energy calculations for metals and semiconductors using a plane-wave basis set. *Comput. Mater. Sci.* **1996**, *6*, 15–50.

(38) Kresse, G.; Furthmüller, J. Efficient iterative schemes for *ab initio* total-energy calculations using a plane-wave basis set. *Phys. Rev. B: Condens. Matter Mater. Phys.* **1996**, *54*, 11169–11186.

(39) Kresse, G.; Joubert, D. From ultrasoft pseudopotentials to the projector augmented-wave method. *Phys. Rev. B: Condens. Matter Mater. Phys.* **1999**, *59*, 1758–1775.

(40) Pei, Y.; Shi, X.; LaLonde, A.; Wang, H.; Chen, L.; Snyder, G. J. Convergence of electronic bands for high performance bulk thermoelectrics. *Nature* **2011**, *473*, 66–69.

(41) Linghu, J.; Shen, L.; Yang, M.; Xu, S.; Feng, Y. P. Si₂₄: An Efficient Solar Cell Material. *J. Phys. Chem. C* **2017**, *121*, 15574–15579.

(42) Arrieta, U.; Katcho, N. A.; Arcelus, O.; Carrasco, J. First-Principles Study of Sodium Intercalation in Crystalline Na_xSi₂₄ (0 ≤ x ≤ 4) as Anode Material for Na-ion Batteries. *Sci. Rep.* **2017**, *7*, 510.

(43) Thomas, J. A.; Iutzi, R. M.; McGaughey, A. J. H. Thermal conductivity and phonon transport in empty and water-filled carbon nanotubes. *Phys. Rev. B: Condens. Matter Mater. Phys.* **2010**, *81*, 045413.

(44) Stefanoski, S.; Malliakas, C. D.; Kanatzidis, M. G.; Nolas, G. S. Synthesis and Structural Characterization of Na_xSi₂₄ (0 < x ≤ 24) Single Crystals and Low-Temperature Transport of Polycrystalline Specimens. *Inorg. Chem.* **2012**, *51*, 8686–8692.

(45) Medeiros, P. V. C.; Stafström, S.; Björk, J. Effects of extrinsic and intrinsic perturbations on the electronic structure of graphene: Retaining an effective primitive cell band structure by band unfolding. *Phys. Rev. B: Condens. Matter Mater. Phys.* **2014**, *89*, 041407.

(46) Medeiros, P. V. C.; Tsirkin, S. S.; Stafström, S.; Björk, J. Unfolding spinor wave functions and expectation values of general operators: Introducing the unfolding-density operator. *Phys. Rev. B: Condens. Matter Mater. Phys.* **2015**, *91*, 041116.